Muon ($g − 2$): Experiment and Theory

James P. Miller,[1] Eduardo de Rafael,[2] B. Lee Roberts,[1] and Dominik Stöckinger[3]

[1]Department of Physics, Boston University, Boston, Massachusetts 02215

[2]Centre de Physique Théorique, CNRS-Luminy, F-13288 Marseille Cedex 9, France

[3]Institut für Kern- und Teilchenphysik, Technische Universität Dresden, D-01062 Dresden, Germany

Keywords

Abstract

We review the status of the theoretical and experimental determinations of the muon magnetic moment anomaly, $a_\mu = (g_\mu − 2)/2$. We discuss future experimental efforts, as well as implications for physics beyond the Standard Model that come from past and future experiments.

Contents

1. INTRODUCTION AND HISTORY OF g FACTORS

The subject of g factors evolved with the "modern physics" of the twentieth century. It was Stern & Gerlach (1–3) who first measured the g value of the electron; however, to determine that they had done so we needed to wait for the invention of spin (4, 5), the development of quantum mechanics (6), and Thomas's (7) relativistic calculation. All of these ingredients were beautifully combined into Dirac's famous 1928 paper (8), in which he introduced his relativistic wave equation. Dirac was surprised to discover that this equation also predicted the electron magnetic moment: "It gave just the properties that one needed for an electron. That was an unexpected bonus for me, completely unexpected" (9). Today we understand that the one Bohr magneton measured in the Stern–Gerlach and Phipps–Taylor (10) experiments represents the magnetic moment of the unpaired atomic electron in silver and hydrogen, respectively. The magnetic dipole moment (MDM) and the (*P*- and *T*-violating) electric dipole moment (EDM) (11–14) are directed along the spin:

$$\vec{\mu} = g\left(\frac{Qe}{2m}\right)\vec{s}; \qquad \vec{d} = \eta\left(\frac{Qe}{2mc}\right)\vec{s}, \qquad\qquad 1.$$

where $Q = \pm 1$, $e > 0$, and the Dirac theory predicts $g \equiv 2$.

In 1948, motivated by measurements of the hyperfine structure of hydrogen that were larger than expected from Dirac theory (15–17), Schwinger (18)[1] showed that "[t]hese discrepancies can be accounted for by a small additional electron spin magnetic moment . . . the radiative correction . . . corresponds to an additional magnetic moment associated with the electron spin of magnitude $\delta_\mu/\mu = \alpha/(2\pi) \simeq 0.001162$." This calculation was the very first loop calculation in quantum field theory. Shortly thereafter, Kusch & Foley (19) reported a 4% measurement of this anomalous moment that agreed well with $\alpha/(2\pi)$. This elegant, mass-independent result is

---

[1]The first paper contains the misprint $(\frac{1}{2})\pi e^2/\hbar c$ for a_e, which is corrected in the second paper.
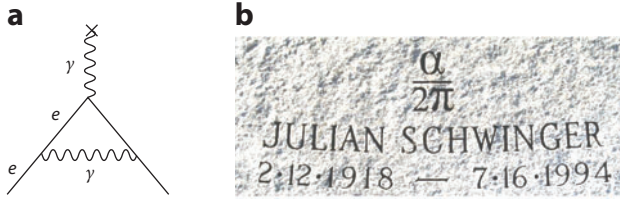
Figure 1

(*a*) One-loop Feynman graph. (*b*) Schwinger's value for this lowest-order correction (18), inscribed on the memorial marker near his grave in the Mount Auburn Cemetery, Cambridge, Massachusetts. Photograph by B.L. Roberts. All rights reserved.

inscribed on the memorial marker located near Schwinger's grave in the Mount Auburn Cemetery in Cambridge, Massachusetts (**Figure 1**).

It is useful to break the magnetic moment into two terms: $\mu = (1 + a)e\hbar/2m$, where $a = (g - 2)/2$. The first term is the Dirac moment in units of the appropriate magneton $e\hbar/2m$. The second term is the anomalous (Pauli) moment (20, p. 51), where the dimensionless quantity a (Schwinger's δ_μ/μ) is sometimes referred to as the anomaly.

The relatively long muon lifetime of $\simeq 2.2$ μs permits precision measurements of its lifetime, magnetic moment, and decay modes. Central to MDM measurements is the production of polarized muons from the weak decay $\pi^- \rightarrow \mu^- \bar{\nu}_\mu$, along with the self-analyzing three-body weak decay $\mu^- \rightarrow e^- \nu_\mu \bar{\nu}_e$, which provides information about the muon spin direction at the time of decay.

The magnetic moment of the muon played an important role in the discovery of the generation structure of the Standard Model (SM). The pioneering muon spin rotation experiment at the Nevis cyclotron observed parity violation in muon decay (21) and showed that g_μ is consistent with the Dirac value of two. Subsequent experiments at Nevis (22) and CERN (23) showed that $a_\mu \approx \alpha/(2\pi)$, implying that in a magnetic field, the muon behaves like a heavy electron. Two additional experiments at CERN required that contributions from higher-order quantum electrodynamics (QED) (24) and then from virtual hadrons (25) be included into the theory in order to reach agreement with experiment (**Figure 2**).

All of these measurements make use of the torque on a dipole in an external field, $\vec{\tau} = \vec{\mu} \times \vec{B} + \vec{d} \times \vec{E}$, where we include the possibility of an EDM. Except for the original Nevis spin rotation experiment, the MDM experiments inject a beam of polarized muons into a magnetic field and measure the rate at which the spin[2] turns relative to the momentum, $\vec{\omega}_a = \vec{\omega}_S - \vec{\omega}_C$, where S and C stand for spin and cyclotron, respectively. Assuming that the velocity is transverse to the magnetic field ($\vec{\beta} \cdot \vec{B} = 0$), one obtains (7, 26)

$$\vec{\omega}_{a\eta} = \vec{\omega}_a + \vec{\omega}_\eta = -\frac{Qe}{m}\left[a_\mu\vec{B} + \left(a_\mu - \left(\frac{m}{p}\right)^2\right)\frac{\vec{\beta} \times \vec{E}}{c}\right] - \eta\frac{Qe}{2m}\left[\frac{\vec{E}}{c} + \vec{\beta} \times \vec{B}\right]. \qquad 2.$$

Important features of this equation are the motional magnetic and electric (E) fields, $\vec{\beta} \times \vec{E}$ and $\vec{\beta} \times \vec{B}$, which are discussed below.

The E821 Collaboration, working at the BNL AGS (Brookhaven National Laboratory Alternating Gradient Synchrotron), used an electric quadrupole field to provide vertical focusing in the storage ring and shimmed the magnetic field to ± 1 ppm uniformity on average. The storage ring was operated at the so-called magic momentum, $p_{\text{magic}} = 3.094$ GeV/c ($\gamma_{\text{magic}} = 29.3$), such

---

[2]In this review, we often use the term spin in place of the more accurate term polarization.
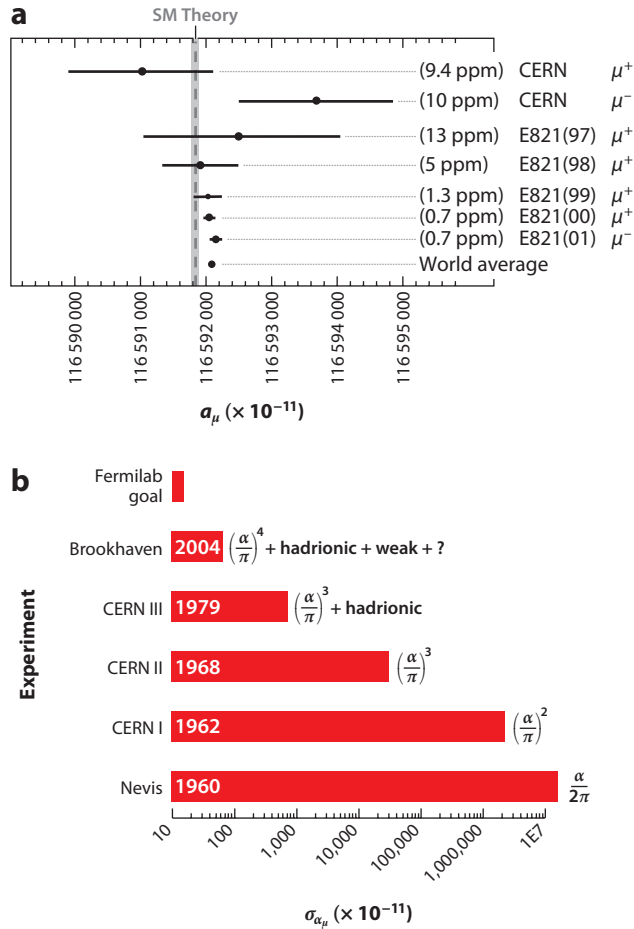
Figure 2

(*a*) Measurements of a_μ. (*b*) The uncertainty on a_μ and the physics reach as the uncertainty decreased. Abbreviation: SM, Standard Model.

that $a_\mu = (m/p)^2$, so the E field did not contribute to ω_a.[3] By measuring the frequency ω_a, and the magnetic field $\vec{B}$ calibrated to the Larmor frequency of the free proton ω_p, one can determine a_μ from the relationship

$$a_\mu = \frac{\omega_a/\omega_p}{\lambda_+ - \omega_a/\omega_p} = \frac{\mathcal{R}}{\lambda_+ - \mathcal{R}}, \qquad 3.$$

where $\lambda_+ = \mu_{\mu^+}/\mu_p = 3.183\ 345\ 137\ (85)$ is the muon-to-proton magnetic moment ratio (27). Assuming *CPT* invariance ($a_{\mu^+} = a_{\mu^-}; \lambda_+ = \lambda_-$), the result is (28, 29)

$$a_\mu^{\text{E821}} = 116\ 592\ 089(54)_{\text{stat}}(33)_{\text{syst}}(63)_{\text{tot}} \times 10^{-11}\ (\pm 0.54\ \text{ppm}). \qquad 4.$$

The muon anomaly is one of the most precisely calculated quantities in the SM. To match the experimental precision, it is necessary to calculate QED contributions to five loops and

---

[3]The magic momentum was first employed by the third CERN collaboration (25).

electroweak (EW) contributions to two loops, all of which are well understood theoretically. It is also necessary to calculate the contributions from hadronic vacuum polarization loops (HVP), as well as from hadronic light-by-light scattering (HLbyL). The HVP contribution can be determined from cross-section data from $e^+e^- \to$ hadrons, whereas that from HLbyL can be determined from models that reproduce the properties of QCD. One recent evaluation (30) obtained

$$a_\mu^{SM} = 116\,591\,802(42)_{HVP}(26)_{HLbyL}(2)_{QED+EW}(49)_{tot} \times 10^{-11}(0.42\text{ ppm}).\qquad 5.$$

Significant progress has been made on lattice calculations, which we expect will play an important role in future determinations of the hadronic contributions.

There is a difference between experimental results and the SM:

$$\Delta a_\mu^{(today)} = a_\mu^{E821} - a_\mu^{SM} = (287 \pm 80) \times 10^{-11},\qquad 6.$$

which could indicate new, as-yet-undiscovered particles, contributing through loops to the muon anomaly. This difference has motivated (*a*) a new experiment at Fermilab, E989, to improve on the E821 result by a factor of four, and (*b*) a proposal at J-PARC that employs a very different technique but has similar goals. The discrepancy has also motivated significant efforts to reduce the uncertainty on the SM value and has been used in many theoretical papers as a constraint on models of New Physics. This difference will continue to be significant in the LHC era and will be one of the important precision-frontier measurements guiding the interpretation of any New Physics discovered at the LHC. Readers interested in a more detailed discussion of these topics than we can provide here are referred to References 31–36.

2. MEASURING a_μ

2.1. Basics of Muon ($g - 2$) Experiments

In the absence of an E field (see Equation 2), the magnetic anomaly can be obtained to a good approximation from $\vec{\omega}_a = -(Qe/m)a_\mu \vec{B}$, the first term in Equation 2. Typically, polarized muons are stored in a circular storage ring that has a fairly uniform magnetic field. The value of a_μ is determined by measuring both the rate of polarization precession, $\vec{\omega}_a$, and the magnetic field, $\vec{B}$, each of which is averaged over the muon ensemble in the ring. Note these two remarkable properties: the rate of precession is proportional to the anomaly, and it is independent of the momentum.

Polarized muons are readily produced via the decay of pions, $\pi^\pm \to \mu^\pm + \nu_\mu(\bar{\nu}_\mu)$, and it is straightforward to select a highly polarized subset of these muons. Large fluxes of pions are produced when energetic protons strike a primary target material. Referring to the pion rest frame, the neutrinos are left handed (helicity $= -1$). Because the pion is spin zero, to conserve angular momentum, the $\mu^\pm$ must have helicities of ∓ 1, respectively. When pions decay in flight, the $\mu^{+(-)}$ that are emitted approximately parallel to the pion momentum (i.e., forward muons) are polarized antiparallel (parallel) to the momentum, whereas those that are emitted antiparallel to the momentum (i.e., backward muons) are polarized parallel (antiparallel) to the momentum. The forward muons are boosted to higher momentum, and the backward muons have a smaller momentum. By selecting the highest, or lowest, momentum muons, one obtains a polarized beam.

A pulsed muon beam is normally used. The temporal width of the muon pulse should be narrow compared with the cyclotron period of the storage ring, and the spacing between pulses should be wide compared with the muon lifetime $\gamma\tau_\mu$. The pulse is injected and stored in a magnetic ring, and the rate of decay electron production is measured as a function of time beginning shortly after injection until the muons have decayed away.

In a storage-ring experiment, some form of kick must be used to place muons on stored orbits in the ring. In the third CERN experiment, 3.2 GeV/c pions were injected into the ring, and the $\pi \to \nu\mu$ decay was used to provide the kick. There were two disadvantages to this technique: (*a*) There was a very low capture efficiency of $\simeq 125$ ppm, which resulted in only $\simeq 350$ stored muons per fill, and (*b*) most of the injected pions did not decay but rather struck the vacuum chamber and other objects, producing neutrons and other particles that created a large background (flash) in the detectors that lasted many microseconds.

Once the muons are stored in the ring, the polarization direction is tracked as a function of time by taking advantage of the correlation between the decay electron direction and the muon spin. The muon decays via the weak interaction, primarily in the mode $\mu^{\pm} \to e^{\pm} + \nu_e(\bar{\nu}_e) + \bar{\nu}_\mu(\nu_\mu)$. The idea can be understood qualitatively as follows for the μ^-. Consider the case in which the decay electron has the maximum possible energy in the muon rest frame. The two neutrinos are emitted at 180° to the electron direction and, with one left handed and the other right handed, have a total spin of zero. Thus the electron carries the muon's spin angular momentum. Left-handed electrons are strongly preferred in the weak decay; thus, the electrons are preferentially emitted antiparallel to the muon spin. One can generalize that, in the rest frame, the higher-momentum electrons are anticorrelated with the spin direction. In the lab frame, there are more high-energy electrons when the muon spin is antiparallel to the muon direction than when it is parallel. Detectors are set up to measure the time and energy of the higher-energy decay electrons. The number of detected electrons versus time oscillates at the polarization precession frequency, ω_a.

Ideally, $\vec{B}$ in the storage ring is as uniform as possible, which has the advantage that the rate of precession of all muons is uniform regardless of their positions in the storage ring. This uniformity reduces the need for high-precision muon trajectory information, which can be difficult to obtain. However, a constant $\vec{B}$ field alone cannot hold the beam in the storage ring; some focusing is required, which generally leads to some trajectory dependence in the precession rate. Early muon $(g-2)$ experiments (23, 24) used a gradient $\vec{B}$ field for focusing in the storage ring. The compromise in the uniformity of $\vec{B}$, together with limited information on the average muon trajectories, represented a limitation on the ultimate sensitivities of the measurements. E821, following the example of the third CERN experiment, employed a highly uniform magnetic field and electric quadrupoles (40) to focus the beam. The E fields are directed transverse to the direction of muon motion and provide weak focusing: $0 < n < 1$, where $n = \frac{\kappa R_0}{\beta B_0}$ and κ is the electric quadrupole gradient. The stored muon beam has a betatron structure typical of a weak-focused beam: The stored particles undergo simple harmonic motion in the radial and vertical dimensions as the beam alternately focuses and defocuses.

Because the electric quadrupole field is position dependent, the rate of precession likewise depends on position, even when the $\vec{B}$ field is highly uniform (see Equation 2). To regain as uniform a rate of polarization precession as possible, both the CERN and E821 experiments stored muons at approximately the magic momentum, $p = 3.094\,\mathrm{GeV}/c$, where $a_\mu = (m/p)^2$ and the precession due to the E field is minimized. In E821, collimators limited the range of stored muon momenta to $\pm 0.25\%$ to minimize the uncertainty in the precession rate due to the $\vec{E}$ field and the modest information available on the muon trajectories.

At the magic momentum, the electrons from muon decay range in energy from zero to 3.1 GeV/c. Most of these electrons have momenta that are less than those of the muon, and the magnetic field deflects these electrons to a smaller radius in the storage ring, where they can be detected. The experimental observable is the number of detected high-energy electrons (nominally above ~1.8 GeV) as a function of time, which oscillates at the same rate as the muon precession frequency.
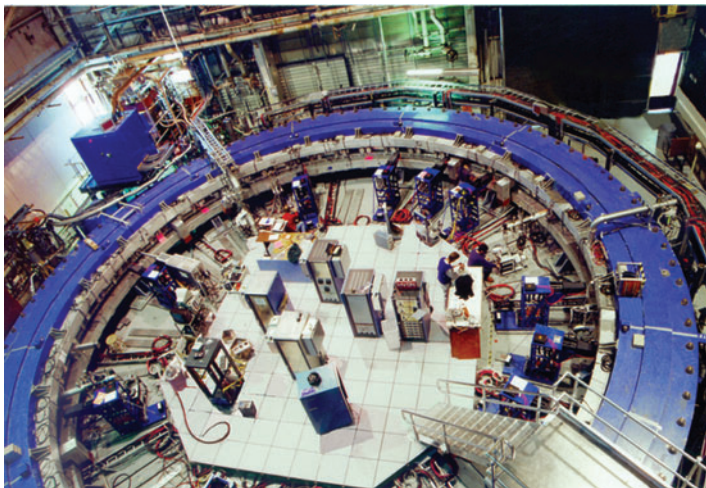
Figure 3

The E821 storage ring. Three adjacent calorimeters can be seen at the top of the photo on the inside of the ring. Reproduced courtesy of Brookhaven National Laboratory.

All past muon ($g - 2$) experiments have used ferric magnets. The third CERN experiment and the E821 experiment used extensive shimming techniques to achieve the desired uniform $\vec{B}$. Given that the ferric fields are limited in practice to $\approx$1.5 T, it follows that the ring diameter for 3.096 GeV/c muons is $\approx$14 m. At this field, the spin precession frequency is approximately 223 kHz, and there are 150 rotations of the polarization during the 10-muon lifetime measurement period of 640 μs. **Figure 3** shows the E821 storage ring. **Figure 4a** shows a cross section of the E821 storage-ring magnet. The CERN experiment used room-temperature copper coils in its magnet. E821 opted for superconducting coils, which allow the magnet to reach equilibrium in a few minutes because there is no Joule heating of the coils and magnet yoke; this magnet provides better temporal stability in the $\vec{B}$ field.

2.2. The Brookhaven Experiment E821

For E821 to improve on the CERN measurement, a much larger statistical sample of muons was required, and both the low stored-muon beam intensity and flash problems had to be solved. To address these issues, a new approach was developed for the BNL ($g - 2$) experiment. The AGS delivered 24 GeV/c protons that struck a primary target. Pions with a momentum of approximately 3.2 GeV/c were collected and directed by dipole magnets into a straight section of alternating quadrupoles that maintained a pion focus and collected highly polarized ($P = 95\%$) forward muons. This beam was sent through a momentum-selection dipole system, producing a beam[4] of the magic momentum that was injected directly into a circular storage ring through the use of a septum magnet known as the inflector (**Figure 4**) (37). A magnetic pulsed kicker (38), acting inside the storage-ring aperture, supplied the 10-mrad kick needed to deflect the injected muons into stable orbits, storing several thousand muons per fill of the ring. Direct muon injection greatly reduced the injection flash in the detectors and significantly improved the number of stored muons

---

[4]The μ^+ beam composition was $\mu^+ : \pi^+ : e^+ : p \simeq 3 : 3 : 3 : 1$; the μ^- beam contained equal numbers of μ^-, π^-, and e^-.
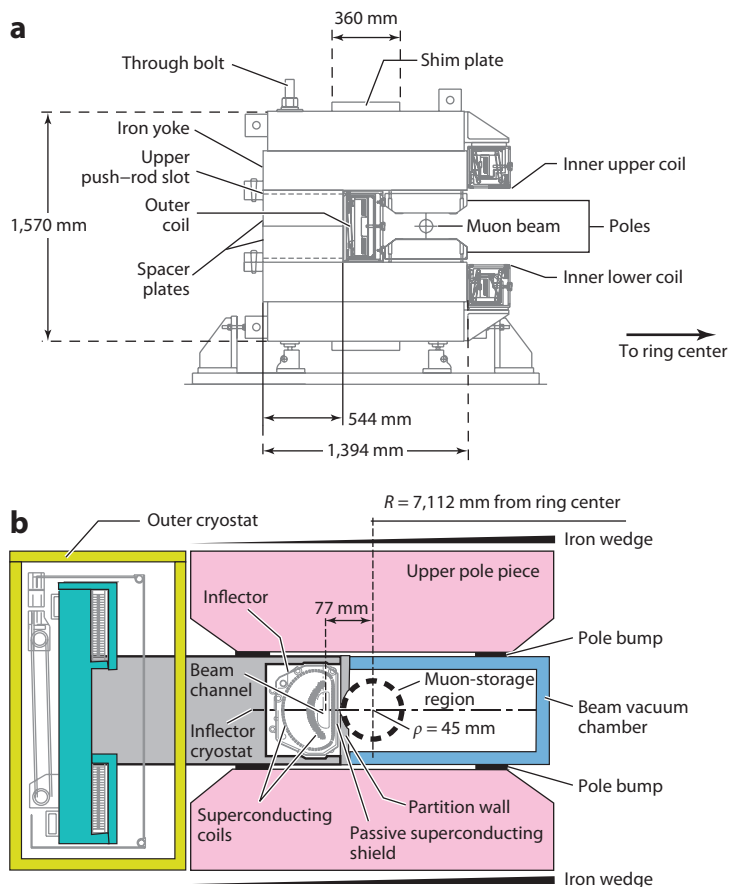
Figure 4

(*a*) Cross-sectional view of the C magnet. The ring center is at the right. Reprinted with permission from Reference 29. Copyright 2006, the American Physical Society. (*b*) The geometry where the beam enters the storage ring through the inflector magnet. The downstream end of the inflector is shown; the beam channel is to the left of the storage region (at a larger radius). The current in the inflector flows into the page in the C-shaped arrangement of conductors just to the left of the beam channel and out of the page in the conductors that form a backward D.

compared with the pion-injection technique used at CERN and in the first E821 data-collection period (25, 39). Nevertheless, the muon-injection flash was still large enough to require that the photomultipliers in the detectors be gated off near the injection point in the ring for 10 to 20 μs following injection to ameliorate the effects of the flash.

It was important to minimize muon losses from the storage ring during the data-collection period. The main source of polarized muons is from pion decays in the straight decay section of the beam line. A secondary source consists of muons produced just downstream of the production target before entering the straight section. As these muons pass through the first dipole region, their spins precess. Therefore, the two sources have slightly different spin phases and are likely to have different loss rates in the storage ring because of their different phase spaces. This difference can cause a shift in the polarization phase of stored muons at late times compared with early storage times, which leads to a distortion in the value of the precession frequency. There was no way to

quantify the differences in initial phase or loss rates. Instead, measures were taken to minimize muon losses. Most lost muons have trajectories passing close to the storage-ring collimators; therefore, these are eliminated shortly after injection by "scraping" the beam (29).

2.2.1. Measurement of the spin rotation frequency. The observable of interest was the oscillation frequency in the rate of detected high-energy electrons as a function of time, which is equal to the spin rotation frequency. The electrons were detected by 24 electromagnetic calorimeters (41) that were evenly spaced around the 45-m circumference of the ring. The positions and size of the calorimeters were optimized to efficiently detect decay electrons with the largest decay asymmetry, namely electrons above approximately 1.8 GeV. The storage-ring vacuum chamber was scalloped so that the decay electrons passed nearly normal to the vacuum wall, directly into the calorimeters. The phototubes viewing the calorimeter were read out by eight-bit 400-MHz waveform digitizers (WFDs) that provided time and energy information about the electron or positron.

Time histograms of high-energy electron data from each calorimeter follow the basic parent distribution of an oscillation at the precession frequency, decaying away with the muon lifetime

$$N(t) = N_0 e^{-t/\gamma\tau_\mu}[1 + A\cos(\omega_a t + \phi)], \qquad\qquad 7.$$

where $\gamma\tau_\mu \approx 64.4$ μs is the dilated muon lifetime, $A \approx 0.3$ is the asymmetry, $\omega_a \approx 2\pi \times 233$ kHz is the angular precession frequency of the polarization, and ϕ is the phase. **Figure 5** shows a histogram of the 2001 data for electrons above 1.8 GeV.

Any shift in the fitted pulse times registered at early times in the injection period compared with late times (early-to-late shifts, for short) leads to a shift in the phase ϕ. The phase also depends on the electron energy; therefore, an early-to-late systematic shift in the gain also shifts ϕ. Because ϕ is highly correlated to ω_a, an unaccounted-for early-to-late shift in ϕ leads to a systematic error in ω_a and, in turn, in a_μ. Such potential sources of early-to-late effects must be minimized.

To control phase shifts, each photomultiplier/WFD combination must be stable against time and pulse-amplitude drifts as a function of time after injection. In E821, the pulse timing, on average, was stable to better than 20 ps over any 200-μs time interval and kept the systematic error contribution to a_μ under 0.1 ppm. Typically, the average timing was stable to 10 ps, early to
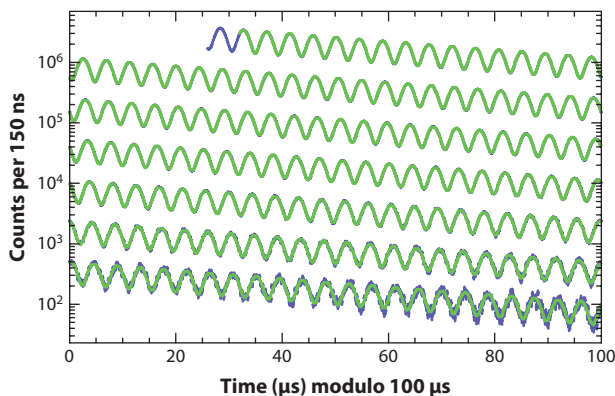

Figure 5

Histogram, modulo 100 μs, of the number of detected electrons above 1.8 GeV for the 2001 data set as a function of time, summed over detectors. A least-squares fit to the spectrum is superimposed. The total number of electrons is 3.6×10^9. Reproduced courtesy of the E821 Collaboration.

late. A shift in the gain of the detectors shifts the apparent energy of the electron, causing a shift in phase. The gain was stable to better than 0.2% over 200 μs and kept the systematic error under 0.1 ppm.

Data rates in the calorimeters were high enough that it was necessary to consider the effect of two electron pulses overlapping in time (this effect is known as pileup). For each injection period, approximately 20 electrons above 1.8 GeV were collected in each calorimeter. The instantaneous rate of electrons above 1 GeV in a single calorimeter varied from ∼300 kHz to zero Hz, early to late; thus, the probability of pileup varied as a function of time after injection and could lead to an early-to-late effect. If two pulses were too close together in time in a given calorimeter, they could be mistaken as a single pulse. Such an error results in the loss of one of the two pulses and an incorrect energy assignment. Pileup effects were modeled and the time histograms were corrected for pileup before least-square fits were performed. Limitations in this modeling procedure led to a systematic error of 0.08 ppm.

The (betatron) frequencies of oscillation in the radial (x) and vertical (y) dimensions of the stored beam are given by $f_x = f_C\sqrt{1-n} \approx 0.93 f_C$ and $f_y = f_C\sqrt{n} \approx 0.36 f_C$, where the cyclotron frequency is $f_C = 6.7 \times 10^6$ Hz with $n \approx 0.13$. At early times, the betatron motions of all muons are in phase. The resulting beam oscillations are referred to as coherent betatron oscillations (CBOs), and the radial CBOs can be enhanced if the storage kick is not ideal. The detector acceptance depends on the distribution of the stored muons in the storage aperture. Oscillations in the average beam position and size due to betatron motion lead to oscillations in the acceptance of the detectors, which is thereby embedded in the time histograms by both horizontal and vertical motion. The coherent vertical motion (frequency f_y) is quite high compared with the precession frequency, is small in amplitude, and dephases fairly quickly in the measurement period. Even though the vertical CBO disappears rather quickly, the individual beam particles continue to undergo vertical oscillations. A small term proportional to $\vec{\beta} \cdot \vec{B}\vec{\beta}$ has been omitted from Equation 2. The component $\beta_y^2 B$ is always positive and leads to a small shift in ω_a due to vertical betatron oscillations—the pitch correction (31). This correction is applied later in the calculation of a_μ. Because of the narrow horizontal inflector aperture (**Figure 4**), the horizontal focus "marches" around the ring at the frequency $f_{CBO} = f_C - f_x \approx 0.07 f_C \approx 470$ kHz and can persist for hundreds of microseconds. This frequency is close to twice the precession frequency ω_a, and if the difference frequency $\omega_{CBO} - \omega_a$ is close to ω_a, then the derived value of ω_a shifts if the betatron motion is not accurately modeled in the fitting procedure. Limitations in the modeling of the required small modifications to the fitting function, which are mainly the result of uncertainties on the muon trajectories, lead to f_{CBO}-related CBO systematic errors of 0.07 ppm.

Some knowledge of the muon trajectories is required in order to calculate the average magnetic field, obtain information on the betatron oscillations, and search for a muon EDM. In the fast rotation method, one observes how the initial spatially bunched stored-muon beam spreads out as a function of time after injection. All muons travel near the speed of light, but the low-momentum muons have a lower average storage radius than do the high-momentum muons; therefore, the former have smaller cyclotron periods. The fast rotation analysis gives the distribution of cyclotron periods and, indirectly, the distributions of the momenta and average radii of curvature of the stored muons.

A straw-tube array at one E821 detector station was used to trace electrons back through the magnetic field from the detector to the point at which their trajectories were tangent to the storage ring, which is a good approximation to where they were "born." These trace-back chambers provided sufficient trajectory and momentum information to trace back to within 0.9 cm and 1.5 cm of the vertical and radial position, respectively, the point where the electron was created, thereby providing a measure of the muon decay locations.

2.2.2. The precision magnetic field. To determine the muon anomaly to the sub-parts-per-million level, it is necessary to know the magnetic field averaged over the muon distribution to a fraction of a part per million. Numerous quantities must be known to achieve this goal: the muon distribution; the relative magnetic field everywhere in the storage ring; the magnetic field stability with time; and the absolute calibration of the magnetic field, which is expressed in terms of the Larmor precession frequency of a free proton, ω_p.

The magnetic field averaged over the muon distribution (see Equation 2) is $\langle B \rangle_{\mu-\text{dist}} = \int M(r,\theta) B(r,\theta) r \, dr \, d\theta$, where $M(r,\theta)$ is the muon distribution and $B(r,\theta) = \sum_{n=0}^{n=\infty} r^n (c_n \cos n\theta + s_n \sin n\theta)$, which is, in practice, limited to five terms. The muon distribution $M(r,\theta)$ is approximately circular, with small higher moments that couple term by term to the field multipoles. The radial and vertical betatron wavelengths are $\lambda_x \simeq 1.08(2\pi R)$ and $\lambda_y \simeq 2.7(2\pi R)$, respectively, so the circulating muons average the field over the entire azimuth of the ring. Furthermore, the use of electrostatic quadrupoles for vertical focusing frees the magnet designer to produce a very uniform magnetic dipole field. The quadrupole and sextupole moments at the edge of the aperture are at the 1 to 2 ppm level (29). This excellent field uniformity, combined with the circular beam, permitted the determination of $\langle B \rangle$ to a precision of ± 30 ppb.

The storage-ring magnet (**Figure 4a**) (42) had many magnetic shimming tools built into its design. The C-magnet design was necessary to permit the decay electrons to reach the detectors located on the inside of the ring. The asymmetry of the yoke relative to the magnet gap introduced a quadrupole component into the magnetic field. To remove this quadrupole component, steel wedges with an angle of ~50 mrad were placed in the air gap between the pole pieces and the magnet yoke (**Figure 4b**). The steel bumps on the edge of the pole pieces just outside of the vacuum chamber were custom ground to minimize the sextupole component. After mechanical shimming, the higher multipoles were found to be fairly constant in azimuth; they were shimmed out on average by adjusting currents in conductors placed on printed circuit boards going around the ring in concentric circles spaced 2.5 mm apart. These boards were glued to the top and bottom pole faces between the edge shims and were connected at the pole ends to form a total of 240 concentric circles of conductor, connected in groups of four.

Special nuclear magnetic resonance (NMR) probes (29, 43) were used to measure and to monitor the magnetic field during the experiment. Three types of probes were used: a spherical water probe that provided the absolute calibration to the free proton; cylindrical probes to monitor the field during data collection and in an NMR trolley to map the field; and a smaller spherical probe, which could be plunged into the muon-storage region by means of a bellows system to transfer the absolute calibration to the trolley probes. A collection of 360 cylindrical probes placed in grooves on the top and bottom of the muon beam vacuum chamber gave a point-to-point measure of the magnetic field while the beam was in the storage ring. The field-mapping trolley contained 17 cylindrical probes arranged in concentric circles (**Figure 6**). At several-day intervals during the running periods, the beam was turned off, and the field-mapping trolley was driven around inside the evacuated beam chamber, measuring the magnetic field with each of the 17 trolley probes at 6,000 locations around the ring. **Figure 6b** shows one of the resulting field maps, averaged over azimuth.

The absolute calibration utilizes a probe containing a spherical water sample (44). The Larmor frequency of a proton in a spherical water sample is related to that of the free proton through $f_L(\text{sph} - H_2O, T) = [1 - \sigma(H_2O, T)] f_L(\text{free})$ (45, 46), where $\sigma(H_2O, T) = 25.790(14) \times 10^{-6}$ is from the diamagnetic shielding of the proton in the water molecule, determined from (47)

$$\sigma(H_2O, 34.7°C) = 1 - \frac{g_p(H_2O, 34.7°C)}{g_J(H)} \frac{g_J(H)}{g_p(H)} \frac{g_p(H)}{g_p(\text{free})}. \qquad 8.$$
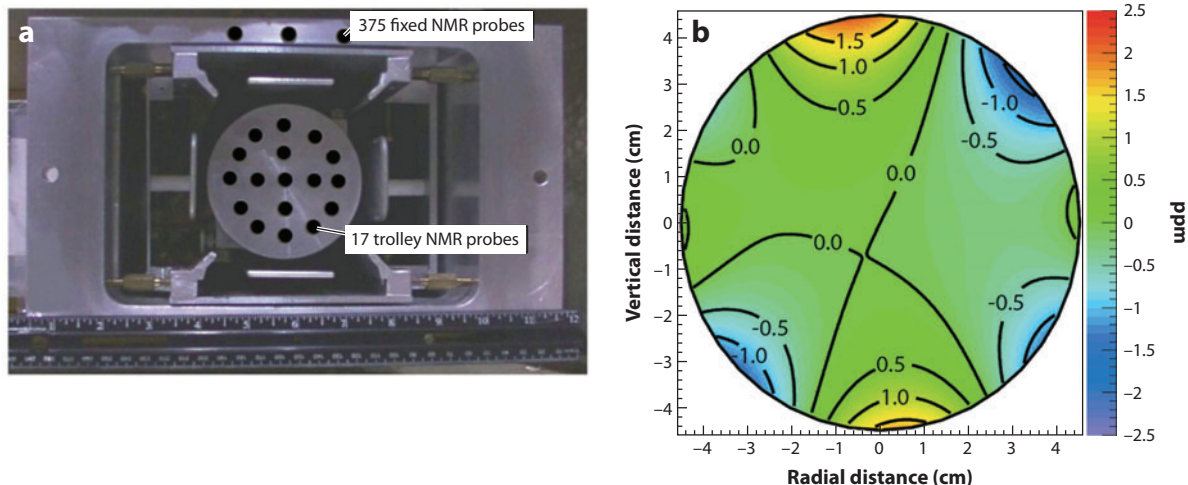
Figure 6

(*a*) The electrostatic quadrupole assembly inside a vacuum chamber showing the nuclear magnetic resonance (NMR) trolley sitting on the rails of the cage assembly. Seventeen NMR probes are located just behind the front face in the places indicated by the black circles. The inner (outer) circle of probes has a diameter of 3.5 cm (7 cm) at the probe centers. The storage region has a diameter of 9 cm. The vertical location of 3 of the 180 upper fixed probes is also shown. An additional 180 probes are located symmetrically below the vacuum chamber. Reproduced courtesy of Y. Semertzidis, Brookhaven National Laboratory. (*b*) A contour plot of the magnetic field averaged over azimuth. The intervals are 0.5 ppm. Reproduced courtesy of the E821 Collaboration.

The terms are (*a*) the ratio of the *g* factors of the proton in a spherical water sample to that of the electron in the hydrogen ground state [g_J(H)] (47); (*b*) the ratio of electron-to-proton *g* factors in hydrogen (48); and (*c*) the bound-state correction relating the *g* factor of the proton bound in hydrogen to the free proton (49, 50). The temperature dependence is from Reference 51. The free proton frequency is determined to an accuracy of ± 0.05 ppm.

2.3. Determination of a_μ

The value of a_μ was extracted from two measured quantities: the muon precession rate, ω_a, determined from fits to the time spectra of decay electrons, and the magnetic field maps calibrated to the Larmor precession frequency of the free proton, ω_p. Each was averaged over time and position in the ring, weighted by the positions and populations of the muons. To avoid uncertainties in the conversion of ω_p to B and in the uncertainty of the muon mass, a_μ was calculated from the frequency ratio $\mathcal{R}$ by use of Equation 3. In E821 the values of ω_a and ω_p were established by independent teams, and a blind analysis scheme was followed. All intermediate values of ω_a and ω_p were reported with hidden constant offsets, and no collaboration member knew both. The offsets were revealed only after both sets of analyses were complete, so intermediate calculations of a_μ were not possible.

The time standard for ω_a is established by the WFDs, which are driven by a 200-MHz clock. The time standard for ω_p is established by the NMR driver frequency. Both frequencies are stabilized by the same frequency standard, so any uncertainty in the absolute frequency of the standard cancels when deducing a_μ. After the offsets were revealed, the following corrections were made to ω_a: (*a*) an E field–related correction of approximately 0.5 ppm, due to the $\vec{\beta} \times \vec{B}$ term in Equation 2, to account for the fact that not all muons had the magic momentum, and (*b*)

a pitch correction of approximately 0.3 ppm, due to vertical betatron motion. Then the value of a_μ was calculated with no further changes.

The values of $\mathcal{R} = \frac{\omega_a}{\omega_p}$ (see Equation 3), after pitch and E-field corrections, are (29) $\mathcal{R}_{\mu^+} = 0.003\,707\,204\,7(26)$ and $\mathcal{R}_{\mu^-} = 0.003\,707\,208\,3(26)$. The difference, $\mathcal{R}^- - \mathcal{R}^+ = (3.6 \pm 3.7) \times 10^{-9}$, is consistent with zero, in accord with the *CPT* theorem.

The frequency ratio $\mathcal{R}$ is model independent, but the determination of a_μ requires λ_+, which is determined from the hyperfine structure of the $\mu^+ e^-$ atom. Thus, the computation of a_{μ^-} from Equation 3 by necessity assumes *CPT* invariance. Using this assumption, we combine $\mathcal{R}^-$ and $\mathcal{R}^+$ to obtain $\mathcal{R}_\mu = 0.003\,707\,206\,3(20)$, yielding $a_\mu^{E821} = 116\,592\,089(63) \times 10^{-11}$ (Equation 4), where we have used the value for λ_+ (27) that was updated in 2008. That value increased a_μ^{E821} by 9×10^{-11} compared with the published value (29).

2.4. The Permanent Electric Dipole Moment

At present, all the measured values of permanent EDMs for elementary particles, including the muon, are consistent with zero. A new limit on the muon EDM (52) was obtained as a secondary result in E821. If the muon EDM were nonzero, there would be an additional term, ω_η, in the expression for the precession frequency given in Equation 2. To good approximation, ω_a is directed parallel to the $\vec{B}$ field, and ω_η is directed radially because the $\vec{\beta} \times \vec{B}$ term dominates. The net effects of the EDM are to tip the plane of polarization precession out of the ring plane by the angle $\delta = \tan^{-1}\frac{\eta\beta}{2a_\mu}$ and to increase the magnitude of the precession according to $\omega = \sqrt{\omega_a^2 + \omega_\eta^2} = \sqrt{\omega_a^2 + (\frac{e\eta\beta B}{2m})^2}$. This tipping causes the average vertical component of the momentum of the decay electron to oscillate with frequency ω_a, but out of phase with ω_a by $\pi/2$. Observed limits on the oscillation in the average vertical position of electrons entering the calorimeters, obtained through the use of position-sensitive scintillators placed in the entrance face of the calorimeters, as well as oscillation of the angle of the electron trajectory to the ring plane from the traceback data, give the result $d_\mu = (0.0 \pm 0.9) \times 10^{-19}$ ecm. The 95%-CL limit is $|d_\mu| < 1.8 \times 10^{-19}$ ecm (52). The presence of an EDM increases the measured frequency, and in principle the observed positive value of Δa_μ (Equation 6) can be attributed to a nonzero EDM. The value of d_μ would shift the value of a_μ by $\delta a_\mu(d_\mu) = (0.0 \pm 42) \times 10^{-11}$, which is much smaller than the observed Δa_μ. We conclude that the EDM is probably not the source of the large positive value for Δa_μ.

3. FUTURE EXPERIMENTS

To clarify the apparent difference between experiment and theory, a new experiment, E989, that reuses the precision storage ring developed at BNL is being prepared at Fermilab (53). The $(g - 2)$ ring and the Mu2e experiments will be located on the new Muon Campus at Fermilab (**Figure 7**).

The goal is a factor-of-four improvement in precision over that of E821, with equal systematic and statistical uncertainties of ± 0.1 ppm, combining to an overall uncertainty of ± 0.14 ppm. This improvement will require $\sim 2 \times 10^{11}$ analyzed events, 21 times the number of events in E821. The final E821 ω_p and ω_a systematic errors were ± 0.17 ppm and ± 0.21 ppm, respectively (29), so both systematic errors will need to be improved by a factor of approximately three.

The baseline proposal is to focus on a_{μ^+}, given that the π^+ production cross section is 2.5 times larger than for π^- at a proton energy of 8 GeV/c. The current plan is to use 4 out of 20 batches in a booster cycle—the others are used by the neutrino program—and subsequently divide each batch into 4 smaller "bunches" of 1×10^{12} protons each. One bunch at a time is extracted
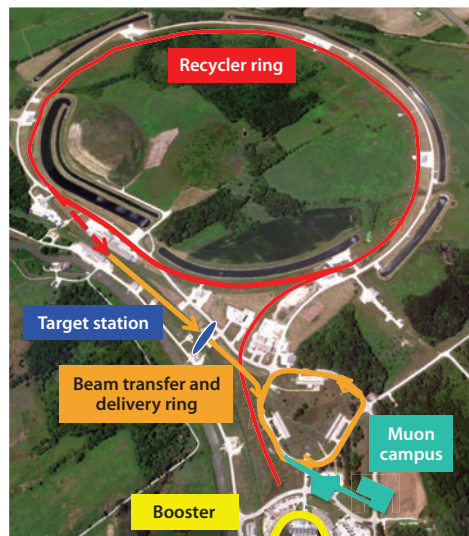
Figure 7

The proposed layout of the proton beam and Muon Campus at Fermilab. The smaller building is the $(g - 2)$ hall. Reproduced courtesy of M. Convery, Fermilab.

and brought to the pion production target at the location of the former antiproton production target. The resulting intense pion beam will be injected into the former antiproton debuncher ring—which has been renamed the delivery ring (DR)—for three turns, then sent on to the $(g - 2)$ storage ring.

The total muon path length is 1,900 m, so most of the pions in the beam will decay before arriving at the ring. However, a significant number of protons from the production target will be present. The speed of protons is ∼5% less than the speed of muons, so after three turns in the DR the proton and muon arrival times differ by ∼250 ns, and the protons can be diverted by a fast kicker before the muon beam is extracted from the DR. Both the pion- and proton-induced flashes will be reduced significantly compared with those in E821. This arrangement will permit E989 to use a pion momentum that is much closer to p_{magic}, which will result in increased flux and higher polarization. Overall, we expect an improvement of a factor of six in the number of stored muons per proton on target in the new experiment compared with E821.

Every aspect of the experiment will be improved over E821: The magnetic field will be better shimmed, the fast muon kicker in the storage ring will be upgraded, the detectors will be segmented, the electronics will be upgraded, and the field measurement and control hardware will also be refurbished and upgraded. A new traceback system will be implemented; it should provide an improvement of two orders of magnitude on the muon EDM and should also yield information on the stored muon distribution. E989 received approval from Fermilab in January 2011, and Fermilab management is working with the US Department of Energy to develop a funding schedule. It is expected that the storage ring will be moved in the fall of 2013, and the first beam could be taken in early 2016.

An alternate approach has been proposed at J-PARC, which uses a much lower muon energy and does not employ the magic momentum technique (**Figure 8**) (54). A surface muon beam produced by the 3 GeV/c booster will be brought to rest in an aerogel target, where muonium (the $\mu^+ e^-$ atom) will be formed. The muonium will be ionized by a powerful laser that produces a very slow
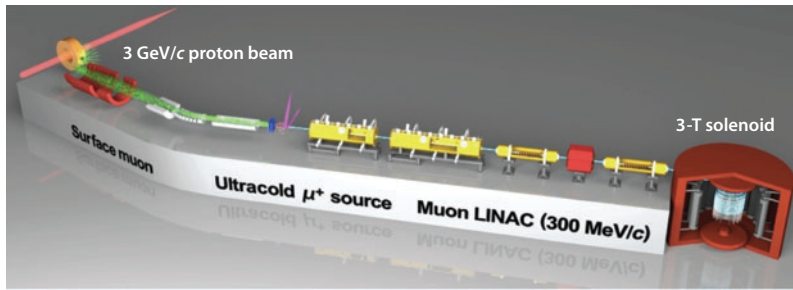
Figure 8

The layout of the proposed J-PARC experiment. Reproduced courtesy of N. Saito, KEK.

muon beam with extremely small emittance. This low emittance beam will then be accelerated by a linac to 300 MeV/c and injected into a $\sim$1-m-diameter solenoidal magnet with a point-to-point uniformity of ± 1 ppm. The decays will be detected by an array of silicon detectors, which will reconstruct the muon distribution as well as provide time and energy information on the decay e^+. The experimenters estimate a sensitivity comparable to that of E989, but this measurement is still in the early stages of development.

4. THE STANDARD MODEL PREDICTION

The question we discuss in this section is: How well can the SM digest the experimental result quoted in Equation 4? The precision of this measurement is such that it is sensitive to the three couplings of the gauge theory that defines the SM, as well as to its full particle content.[5]

4.1. The QED Contributions (Leptons)

QED contributions are by far the dominant ones. They are generated by two types of Feynman diagrams.

4.1.1. The massless class. This class consists of Feynman diagrams with virtual photons only, as well as diagrams with virtual photons and fermion loops of the same flavor as the external particle (the muon in our case). Because the anomalous magnetic moment is a dimensionless quantity, this class of diagrams gives rise to a contribution that is the same for the muon, electron, and tau anomalies. It corresponds to the entries $a^{(2n)}$ in **Table 1**, where $n = 1, 2, 3,$ or 4 indicates the number of loops involved. The entries at one loop (18), two loops (56, 57), and three loops (58), are known analytically, which is why there is no error quoted in the corresponding numbers in the second column of **Table 1**.

At the four-loop level, there are 891 Feynman diagrams of this type. Some of them are already known analytically, but in general one has to resort to numerical methods for a complete evaluation. Such impressive calculations, which are being systematically pursued by Kinoshita and collaborators (59), require many technical skills and are being constantly updated, thanks in particular to the advances in computing technology. The entry $a^{(8)}$ in **Table 1** is the one corresponding to the most recent published value (59); the error is due to the present numerical uncertainties.

---

[5]For recent review articles see, for instance, References 31 and 55.

Table 1 QED contributions (leptons)[a]

Contribution	Result in powers of $\frac{\alpha}{\pi}$	Numerical value in 10^{-11} units
$a_\mu^{(2)}$	$0.5 \left(\frac{\alpha}{\pi}\right)$	116 140 973.29 (0.04)
$a_\mu^{(4)}$	$-0.328\,478\,965\,(00)\left(\frac{\alpha}{\pi}\right)^2$	—
$a_\mu^{(4)}(m_\mu/m_e)_{VP}$	$1.094\,258\,311\,(08)\left(\frac{\alpha}{\pi}\right)^2$	—
$a_\mu^{(4)}(m_\mu/m_\tau)_{VP}$	$0.000\,078\,064\,(26)\left(\frac{\alpha}{\pi}\right)^2$	—
$a_\mu^{(4)}$(total)	$0.765\,857\,410\,(27)\left(\frac{\alpha}{\pi}\right)^2$	413 217.62 (0.01)
$a_\mu^{(6)}$	$1.181\,241\,46\,(00)\left(\frac{\alpha}{\pi}\right)^3$	—
$a_\mu^{(6)}(m_\mu/m_e)_{VP}$	$1.920\,455\,13\,(03)\left(\frac{\alpha}{\pi}\right)^3$	—
$a_\mu^{(6)}(m_\mu/m_\tau)_{VP}$	$-0.001\,782\,33\,(48)\left(\frac{\alpha}{\pi}\right)^3$	—
$a_\mu^{(6)}(m_\mu/m_e, m_\mu/m_\tau)_{VP}$	$0.000\,527\,66\,(17)\left(\frac{\alpha}{\pi}\right)^3$	—
$a_\mu^{(6)}(m_\mu/m_e)_{LbyL}$	$20.947\,924\,89\,(16)\left(\frac{\alpha}{\pi}\right)^3$	—
$a_\mu^{(6)}(m_\mu/m_\tau)_{LbyL}$	$0.002\,142\,83\,(69)\left(\frac{\alpha}{\pi}\right)^3$	—
$a_\mu^{(6)}$(total)	$24.050\,509\,64\,(43)\left(\frac{\alpha}{\pi}\right)^3$	30 141.90 (0.00)
$a_\mu^{(8)}$	$-1.914\,4\,(35)\left(\frac{\alpha}{\pi}\right)^4$	—
$a_\mu^{(8)}(m_\mu/m_e)_{VP}$	$10.839\,2\,(41)\left(\frac{\alpha}{\pi}\right)^4$	—
$a_\mu^{(8)}(m_\mu/m_e, m_\mu/m_\tau)_{VP}$	$-0.046\,2\,(00)\left(\frac{\alpha}{\pi}\right)^4$	—
$a_\mu^{(8)}(m_\mu/m_e)_{LbyL}$	$121.843\,1\,(59)\left(\frac{\alpha}{\pi}\right)^4$	—
$a_\mu^{(8)}(m_\mu/m_e, m_\mu/m_\tau)_{LbyL}$	$0.083\,8\,(01)\left(\frac{\alpha}{\pi}\right)^4$	—
$a_\mu^{(8)}$(total)	$130.805\,5\,(80)\left(\frac{\alpha}{\pi}\right)^4$	381.33 (0.02)
$a_\mu^{(10)}$(total estimate)	$663\,(20)\left(\frac{\alpha}{\pi}\right)^5$	4.48 (0.14)
$a_\mu^{(2+4+6+8+10)}$(QED)	—	116 584 718.09 (0.14) (0.04)

[a]$\alpha^{-1} = 137.035\,999\,084\,(51)$ (0.37 ppb). Abbreviations: LbyL, light by light; QED, quantum electrodynamics; VP, vacuum polarization.

Note the alternating sign of the results from the contributions of one loop to four loops, a simple feature that is not yet understood from first principles. Also, the fact that the sizes of the $(\alpha/\pi)^n$ coefficients for $n = 1, 2, 3,$ or 4 remain rather small supports the expectation that the order of magnitude of the five-loop contribution, from a total of 12,672 Feynman diagrams, may be of $\mathcal{O}(\alpha/\pi)^5 \simeq 7 \times 10^{-14}$. This value is well beyond the accuracy required for comparison with the present experimental result for a_μ, but it will eventually be needed for an improved determination of the fine-structure constant α from precision measurements of the electron anomaly.[6] The value of α used in **Table 1** is the value extracted from the measured electron $g/2$ factor quoted in Reference 61.

4.1.2. The massive class. This second class is generated by Feynman diagrams with lepton loops whose flavor differs from that of the external muon line. Their contribution to a_μ is then a function of the ratios of lepton masses involved. The relevant diagrams are those generated by vacuum polarization subgraphs and/or by light-by-light scattering subgraphs involving electron and tau loops. **Table 1** gives the results of this evaluation. Both the two-loop and three-loop contributions of this class are known analytically.[7] The full three-loop evaluation involving electron-loop

---

[6]The status of the evaluation of the tenth-order contribution to a_e can be found in Reference 60 and references therein.

[7]For an account of the successive improvements in the evaluation of these contributions, see, for instance, References 31 and 55.
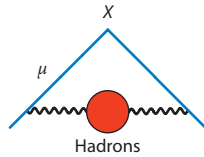
Figure 9

Hadronic vacuum polarization.

subgraphs, by Laporta & Remiddi (62, 63), is a remarkable achievement. The numerical errors quoted in **Table 1** for these contributions are due to the present experimental errors in the lepton masses (64).

At the four-loop level, only a few contributions are known analytically (see Reference 65 and references therein). Kinoshita and his collaborators (see Reference 66 and references therein) have, however, accomplished a full numerical evaluation of this class. The corresponding error in **Table 1** is the combined error in the lepton masses and the present error due to the very many integrals that have been performed numerically. The number quoted for the full five-loop QED contribution in **Table 1** is the estimate quoted in Reference 67, which is being improved.

Kinoshita and collaborators have completed the calculation of all 12,672 diagrams and are preparing the results for publications. After submitting these results for publication, they will continue to increase the precision of the last set with additional computer time (T. Kinoshita, personal communication).

4.2. QED Hadronic Contributions

The electromagnetic interactions between hadrons produces contributions to a_μ that are induced by the HVP and by HLbyL.

4.2.1. Hadronic vacuum polarization. All calculations of the lowest-order HVP contribution to the muon anomaly (**Figure 9**) are based on the spectral representation (68)

$$a_\mu^{\mathrm{HVP}} = \frac{\alpha}{\pi} \int_0^\infty \frac{dt}{t} \int_0^1 dx \frac{x^2(1-x)}{x^2 + \frac{t}{m_\mu^2}(1-x)} \frac{1}{\pi} \mathrm{Im}\Pi(t). \qquad 9.$$

Here, $\frac{1}{\pi}\mathrm{Im}\Pi(t)$ is the hadronic spectral function related to the one-photon e^+e^- annihilation cross section into hadrons as follows ($m_e \to 0$):

$$\sigma(t)_{[e^+e^- \to (\gamma) \to \mathrm{hadrons}]} = \frac{4\pi^2 \alpha}{t} \frac{1}{\pi} \mathrm{Im}\Pi(t). \qquad 10.$$

This contribution is dominated by the $\pi^+\pi^-$ channel, particularly the region of the ρ resonance (69, 70). The history of evaluations of a_μ^{hvp} is a long one that is traced in Reference 31. The most recent compilation of e^+e^- annihilation data used in the evaluation of the dispersive integral in Equation 9, made by Davier and collaborators (30), includes the new $\pi^+\pi^-$ cross-section data from KLOE as well as the available multihadron data from BABAR, and gives the result

$$a_\mu^{\mathrm{HVP}} = [6\,923 \pm 14 \pm 31 \pm 24 \pm 2_\psi \pm 3_{\mathrm{QCD}}(42)_{\mathrm{tot}}] \times 10^{-11} \ [e^+e^- - \mathrm{data}], \qquad 11.$$

where the first error is statistical, the second one is channel-specific systematic, and the third one is common systematic and is correlated with at least one other channel (see Reference 30 and

references therein for details). Another detailed, independent recent analysis (71) gives the result

$$a_\mu^{\text{HVP}} = (6\ 949 \pm 37_{\text{exp}} \pm 21_{\text{rad}}) \times 10^{-11}. \qquad 12.$$

Both determinations are consistent within errors. The updated evaluation corresponding to the one in Equation 11, using the experimental τ-spectral functions quoted in Reference 30, now gives $a_\mu^{\text{HVP}} = (7\ 015 \pm 47) \times 10^{-11}$ [τ − data]; it still deviates from the e^+e^--based evaluation by $1.8\ \sigma$. It has been argued, however, that this deviation practically disappears after correcting the τ data for the $\rho\gamma$ mixing contribution (72, 73).

There exists a similar spectral representation to that in Equation 9 for the next-to-leading order HVP (74); the kernel (75, 76) in Equation 9, $\frac{\alpha}{\pi} \int_0^1 dx \frac{x^2(1-x)}{x^2 + \frac{t}{m_\mu^2}(1-x)}$, is replaced by a two-loop kernel, which is also known analytically (77). Using e^+e^- data, the latest evaluation gives (71)

$$a_\mu^{\text{HVP(NLO)}} = (-98.4 \pm 0.6_{\text{exp}} \pm 0.4_{\text{rad}}) \times 10^{-11}. \qquad 13.$$

A simple explanation for why this contribution turns out to be negative can be found in Reference 31.

Several groups have recently envisaged the possibility of evaluating the contribution to a_μ^{HVP} theoretically, from first principles, by use of lattice QCD. These evaluations use the representation (78, 79)

$$a_\mu^{\text{HVP}} = \frac{\alpha}{\pi} \int_0^1 dx(1-x)\left[-\Pi^{\text{HVP}}\left(-\frac{x^2}{1-x}m_\mu^2 \right) \right], \qquad 14.$$

where $\Pi^{\text{HVP}}(k^2)$ denotes the real part of the renormalized hadronic photon self-energy and the integration here is over the value of this self-energy in the Euclidean region: $0 \le -k^2 = \frac{x^2}{1-x}m_\mu^2 \le \infty$. The first estimates (e.g., Reference 80 and references therein) using this approach are very encouraging. At long range, the lattice QCD approach may become a good test of the determinations using experimental data and, perhaps, may even be competitive in precision.

4.2.2. Hadronic light–by–light scattering.
The standard representation of the contribution to the muon anomaly from the HLbyL process shown in **Figure 10a** is given by the integral (81)

$$a_\mu^{\text{(HLbyL)}} = \frac{-ie^6}{48m_\mu} \int \frac{d^4k_1}{(2\pi)^4} \int \frac{d^4k_2}{(2\pi)^4} \frac{1}{k_1^2 k_2^2 (k_1 + k_2)^2} \left[\frac{\partial}{\partial q^\mu} \Pi_{\lambda\nu\rho\sigma}^{(\text{H})}(q, k_1, k_3, k_2) \right]_{q=0}$$

$$\times \text{tr} \left\{ (\not{p} + m_\mu)[\gamma^\mu, \gamma^\lambda](\not{p} + m_\mu)\gamma^\nu \frac{1}{\not{p} + \not{k_2} - m_\mu}\gamma^\rho \frac{1}{\not{p} - \not{k_1} - m_\mu}\gamma^\sigma \right\}, \qquad 15.$$
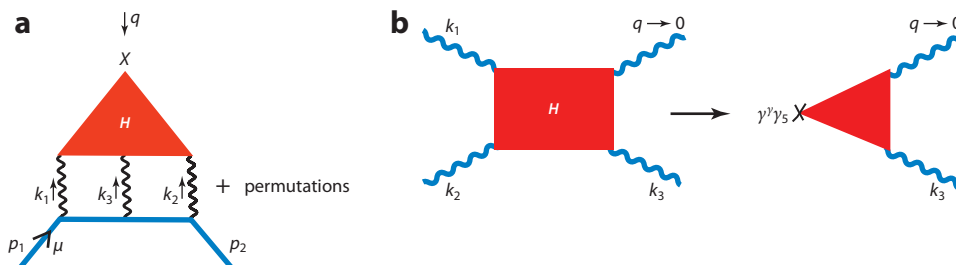

Figure 10

(*a*) Hadronic light-by-light scattering (HLbyL). (*b*) Operator product expansion relation between the HLbyL and axial-vector-vector amplitudes.

where $\Pi^{(H)}_{\mu\nu\rho\sigma}(q, k_1, k_3, k_2)$, with $q = p_2 - p_1 = -k_1 - k_2 - k_3$, denotes the off-shell photon-photon scattering amplitude induced by hadrons. Unlike the HVP contribution, there is no direct experimental input available for the HLbyL amplitude needed to evaluate $a^{(HLbyL)}_{\mu}$; therefore, one has to rely on theoretical approaches. So far, the only known rigorous result is the observation that, in the QCD large-N_c limit and to leading order in the chiral expansion, the dominant contribution comes from Goldstone-like neutral pion exchange, which produces a characteristic universal double logarithmic behavior with a coefficient that has been calculated exactly (82):

$$a^{(HLbyL)}_{\mu}(\pi^0) = \left(\frac{\alpha}{\pi}\right)^3 N_c^2 \frac{m_\mu^2}{48\pi^2 F_\pi^2} \left[\ln^2 \frac{m_\rho}{m_\pi} + \mathcal{O}\left(\ln \frac{m_\rho}{m_\pi}\right) + \mathcal{O}(\text{cte.})\right]. \qquad 16.$$

Here, F_π denotes the pion coupling constant in the chiral limit ($F_\pi \sim 90$ MeV). Testing this limit has been particularly useful in fixing the sign of the phenomenological calculations of the neutral pion-exchange contribution (83). Although the coefficient of the $\ln^2(m_\rho/m_\pi)$ term in Equation 16 is unambiguous, the coefficient of the $\ln(m_\rho/m_\pi)$ term depends on low-energy constants, which are difficult to extract from experiment (82, 84) because doing so requires a detailed knowledge of the $\pi^0 \to e^+e^-$ decay rate with inclusion of radiative corrections. Moreover, the constant term in Equation 16 (not enhanced by large logarithmic factors) is not fixed by chiral symmetry requirements, which makes the predictive power of the chiral perturbation theory approach rather limited for the required accuracy.

A significant improvement in the theoretical knowledge of the HLbyL contribution will be obtained only from a better understanding of the properties of the four-point function $\Pi^{(H)}_{\mu\nu\rho\sigma}(q, k_1, k_3, k_2)$ in QCD, especially its short- and long-distance behaviors. A first step in that direction is the operator product expansion (OPE) constraint discussed by Melnikov & Vainshtein (85). These authors consider a specific kinematic configuration of the virtual photon momenta k_1, k_2, and k_3 in the Euclidean domain. In the limit $q = 0$, these momenta form a triangle: $k_1 + k_2 + k_3 = 0$. In the configuration where one side of this triangle is much shorter than the others, $k_1^2 \approx k_2^2 \gg k_3^2$, and when $k_1^2 \approx k_2^2 \gg m_\rho^2$, one can then apply the known OPE for the product of two electromagnetic currents carrying hard moment k_1 and k_2. In other words,

$$\int d^4x_1 \int d^4x_2 e^{-ik_1\cdot x_1 - ik_2\cdot x_2} J_\nu(x_1)J_\rho(x_2) = \frac{2\varepsilon_{\nu\rho\delta\gamma}\hat{k}^\delta}{\hat{k}^2} \int d^4z e^{-ik_3\cdot z} J_5^\gamma(z) + \mathcal{O}\left(\frac{1}{\hat{k}^3}\right). \qquad 17.$$

Here, $J_5^\gamma = \sum_q Q_q^2 \bar{q}\gamma^\gamma\gamma_5 q$ denotes the axial current, where the sum over different flavors is weighted by squares of their electric charges and $\hat{k} = (k_1 - k_2)/2 \approx k_1 \approx -k_2$. As illustrated in **Figure 10b**, the HLbyL amplitude is reduced, in the special kinematics under consideration, to the axial-vector-vector (AVV) triangle amplitude.

Two observations follow from the OPE relation in Equation 17. First, because only 0^- and 1^+ states can couple to the axial current, the pseudoscalar and pseudovector meson exchanges are the dominant hadronic contributions at large $k_{1,2}$. Second, Equation 17 provides the asymptotic behavior of the vertex form factors at large $k_1^2 \approx k_2^2$; in particular, the $\pi^0\gamma^*\gamma^*$ form factor $\mathcal{F}(k^2, k^2)$ goes as $1/k^2$, and similar asymptotics hold for the axial-vector couplings. This asymptotic behavior has to do with the resulting AVV triangle amplitude, which consists of two parts: the anomalous longitudinal part and its nonanomalous transverse analog. Because of the absence of both perturbative and nonperturbative corrections to the anomalous AVV triangle graph in the chiral limit, the pion pole description for the isovector part of the axial current is correct at all values of k_3^2, thereby connecting regions of soft and hard virtual momenta; it implies the absence of a form factor $\mathcal{F}(0, k_3^2)$ in the vertex, which contains the external magnetic field. Note that this form factor also enters in the transverse component and that it appears with the massless pion pole in the form $\frac{\mathcal{F}(q^2, k_3^2) - \mathcal{F}(0,0)}{(k_3+q)^2}$. At $q = 0$, this combination contains no pion pole at $k_3^2 = 0$, and it

provides the leading short-distance constraint for pseudovector exchange. Contrary to the case of the longitudinal component, the transverse nonanomalous part of the AVV triangle is, however, corrected by nonperturbative contributions (86–88).

Most of the past decade's calculations of $a_\mu^{\text{(HLbyL)}}$ found in the literature (83, 85, 89–94) are compatible with the QCD chiral constraints and the large-N_c limit discussed above. All of them incorporate the π^0-exchange contribution modulated by $\pi^0\gamma^*\gamma^*$ form factors, correctly normalized to the Adler–Bell–Jackiw point-like coupling. They differ, however, on whether or not they satisfy the particular OPE constraint discussed above and in the shape of the vertex form factors that follow from different models: the hidden gauge symmetry model (89), the extended Nambu–Jona-Lasinio (ENJL) model (90), the chiral quark model (91), large-N_c models (83, 85, 92), holographic models (93), and the nonlocal chiral quark model (94). To compare the different results, it is convenient to separate the HLbyL contributions that are leading in the $1/N_c$ expansion from the nonleading ones (79). Among the leading contributions, the π^0 exchange and, to a lesser degree, the η and η' exchanges are the dominant ones. As discussed above, there are good QCD theoretical reasons for this approach. Despite the different choices of the form factors used in the various model calculations, there exists, within errors, a reasonable agreement among the final results.[8] The result quoted in the update discussed in Reference 34 gives

$$a_\mu^{\text{(HLbyL)}}(\pi, \eta, \eta') = (114 \pm 13) \times 10^{-11}. \qquad 18.$$

Other contributions, which are also leading in the $1/N_c$ expansion due to axial-vector exchanges and scalar exchanges, give smaller contributions with updated errors (34):

$$a_\mu^{\text{(HLbyL)}}(1^+) = (15 \pm 10) \times 10^{-11}, \quad \text{and} \quad a_\mu^{\text{(HLbyL)}}(0^+) = -(7 \pm 7) \times 10^{-11}. \qquad 19.$$

The subleading contributions in the $1/N_c$ expansion are dominated by the charged-pion loop. However, because of the model dependence of the results one obtains when the pion loop is dressed with hadronic interactions, the authors of Reference 34 suggested using the central value of the ENJL model evaluation from Reference 90, but with a larger error, which also covers unaccounted-for loops of other mesons:

$$a^{\text{(HLbyL)}}(\pi^+\pi^-) = -(19 \pm 19) \times 10^{-11}. \qquad 20.$$

From these considerations, by adding the errors in quadrature along with the small charm contribution accounted for by a heavy quark loop, $a_\mu^{\text{(HLbyL)}}(c) = 2.3 \pm \times 10^{-11}$, one obtains a final result of

$$a_\mu^{\text{(HLbyL)}} = (105 \pm 26) \times 10^{-11}. \qquad 21.$$

One should keep in mind, however, that this result and the error in particular can be considered only a best estimate at present. Given the proposed new $(g_\mu - 2)$ experiment, it is desirable to have more independent calculations to make this estimate more robust. More experimental information on the decays $\pi^0 \to \gamma\gamma^*$, $\pi^0 \to \gamma^*\gamma^*$, and $\pi^0 \to e^+e^-$ (with radiative corrections included) could also help confirm the result of the main contribution in Equation 18. More theoretical work is certainly needed for a better understanding of the other contributions that, although smaller than the one from pseudoscalar exchanges, nevertheless have large uncertainties. A reliable evaluation of the $1/N_c$ suppressed loop contributions represents an even more difficult task (an initial step

---

[8]An exception is the recent calculation reported in Reference 95, which uses a model based on a Dyson–Schwinger approach. Surprisingly, this result contradicts the simple picture that emerges from the constituent chiral quark model calculations. Furthermore, the treatment in Reference 95, which so far has not included scalar degrees of freedom, is incomplete. For this reason, we do not consider it in the update below.
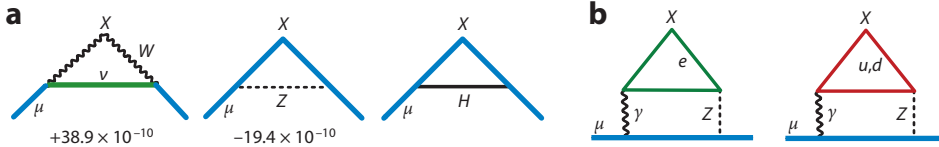
Figure 11

(*a*) Weak interactions at the one-loop level. (*b*) Two-loop electroweak diagrams generated by the $\gamma\gamma Z$ triangle for the first family.

was proposed in Reference 96). New approaches to the dressed pion loop contribution, in parallel with experimental information on the vertex $\pi^+\pi^-\gamma^*\gamma^*$, would be very welcome. Finally, with the development of more and more refined techniques in lattice QCD, there may be first-principle QCD estimates of $a^{(\text{HLbyL})}$ in the near future.

4.3. Electroweak Contributions

The leading contribution to the muon anomaly from the EW Lagrangian of the SM originates at the one-loop level. **Figure 11*a*** shows the relevant Feynman diagrams (in the unitary gauge). The analytic evaluation of the overall contribution gives the result (see, e.g., Reference 97):

$$a_\mu^{\text{EW}(1)} = \frac{G_F}{\sqrt{2}} \frac{m_\mu^2}{8\pi^2} \left\{ \underbrace{\frac{10}{3}}_{W} + \underbrace{\frac{1}{3}(1 - 4\sin^2\theta_W)^2 - \frac{5}{3}}_{Z} + \mathcal{O}\left(\frac{m_\mu^2}{M_Z^2}\log\frac{M_Z^2}{m_\mu^2}\right) \right.$$
$$\left. + \frac{m_\mu^2}{M_H^2}\int_0^1 dx \frac{2x^2(2-x)}{1 - x + \frac{m_\mu^2}{M_H^2}x^2} \right\} = 194.8 \times 10^{-11}, \qquad 22.$$

where the weak mixing angle is defined by $\sin^2\theta_W = 1 - M_W^2/M_Z^2 \simeq 0.223$, and $G_F \simeq 1.166 \times 10^{-5}$ is the Fermi constant. The contribution from the Higgs boson is shown in parametric form in the second line. It is of $\mathcal{O}(\frac{G_F}{\sqrt{2}} \frac{m_\mu^2}{4\pi^2} \frac{m_\mu^2}{M_H^2} \ln \frac{M_H^2}{m_\mu^2})$, which is very small. As a reference, for $M_H = 125$ GeV, this contribution is 2.2×10^{-14}.

The a priori possibility that the two-loop EW corrections may bring in enhancement factors due to large logarithms, such as $\ln(M_Z^2/m_\mu^2) \simeq 13.5$, has motivated a thorough theoretical effort for their evaluation. This evaluation has been a remarkable achievement.

It is convenient to separate the two-loop EW contributions into two sets: those containing closed fermion loops and those containing bosonic corrections, which we denote by $a_\mu^{\text{EW}(2)}(\text{bos})$. The latter have been evaluated using asymptotic techniques in a systematic expansion in powers of $\sin^2\theta_W$, where $\log\frac{M_W^2}{m_\mu^2}$ terms, $\log\frac{M_H^2}{M_W^2}$ terms, $\frac{M_W^2}{M_H^2}\log\frac{M_H^2}{M_W^2}$ terms, $\frac{M_W^2}{M_H^2}$ terms, and constant terms are kept (98–100). By using $\sin^2\theta_W = 0.223$ and the latest LHC results (101), which exclude M_H in the range between 141 and 476 GeV at the 95% CL, and by varying M_H only in the range between 114 and 141 GeV, one obtains

$$a_\mu^{\text{EW}(2)}(\text{bos}) = \frac{G_F}{\sqrt{2}} \frac{m_\mu^2}{8\pi^2} \times \frac{\alpha}{\pi}(-76.4 \pm 1.1) = (-20.7 \pm 0.3) \times 10^{-11}. \qquad 23.$$

The discussion of the fermionic corrections is more delicate. Because of the $U(1)$ anomaly cancellation between lepton loops and quark loops in the EW theory, one cannot separate hadronic from leptonic effects any longer in diagrams such as those in **Figure 11*b***, where a VVA triangle appears. It is therefore appropriate to separate the fermionic corrections into two classes. One

is that shown in **Figure 11b** for the three families; we denote this class $a_\mu^{\text{EW}(2)}(l, q)$. The other class is defined by the remaining diagrams, wherein quark loops and lepton loops can be treated separately; we denote this class $a_\mu^{\text{EW}(2)}(\text{ferm-rest})$. The latter contribution has been estimated to a very good approximation (98) with the result

$$a_\mu^{\text{EW}(2)}(\text{ferm-rest}) = \frac{G_F}{\sqrt{2}} \frac{m_\mu^2}{8\pi^2} \frac{\alpha}{\pi} \times (-21 \pm 4). \qquad 24.$$

Here, the error is that induced by diagrams with Higgs propagators with an allowed Higgs boson mass in the range 114 GeV $< M_H <$ 250 GeV.

Concerning the contributions to $a_\mu^{\text{EW}(2)}(l, q)$, it is convenient to treat the three generations separately. The contribution from the third generation can be calculated in a straightforward way by use of effective field theory techniques (102) because all the fermion masses in the triangle loop are large with respect to the muon mass. The result is (98, 102):

$$a_\mu^{\text{EW}(2)}(\tau, t, b) = \frac{G_F}{\sqrt{2}} \frac{m_\mu^2}{8\pi^2} \frac{\alpha}{\pi} \times (-30.6). \qquad 25.$$

However, as first emphasized in Reference 102, an appropriate QCD calculation when the quark in the loop of **Figure 11b** is light should take into account the dominant effects of spontaneous chiral-symmetry breaking. Because doing so involves the u, d, and s quarks, it is convenient to lump together the contributions from the first and second generations. An evaluation of these contributions, which incorporate the QCD long-distance chiral realization (86, 102), as well as perturbative (103) and nonperturbative (86, 103) short-distance constraints, gives the result

$$a_\mu^{\text{EW}(2)}(e, \mu, u, d, s, c) = \frac{G_F}{\sqrt{2}} \frac{m_\mu^2}{8\pi^2} \frac{\alpha}{\pi} \times (-24.6 \pm 1.8). \qquad 26.$$

Putting together the partial two-loop results discussed above, one finally obtains for the overall EW contribution the value

$$a_\mu^{\text{EW}} = a_\mu^{\text{EW}(1)} + \frac{G_F}{\sqrt{2}} \frac{m_\mu^2}{8\pi^2} \left(\frac{\alpha}{\pi}\right) [-152.6(4.1)(1.8)] = 153(1)(1) \times 10^{-11}. \qquad 27.$$

Here, the first error is essentially due to the mass uncertainty of the Higgs contributions that are not suppressed by a factor of $\frac{m_\mu^2}{M_H^2}$ as in Equation 22; the second error comes from hadronic uncertainties in the VVA loop evaluation. The overall result shows indeed that the two-loop correction represents a sizable reduction of the one-loop result by 21%. An evaluation of the EW three-loop leading terms of $\mathcal{O}[\frac{G_F}{\sqrt{2}} \frac{m_\mu^2}{8\pi^2} (\frac{\alpha}{\pi})^2 \ln \frac{M_Z}{m_\mu}]$, using renormalization group arguments (103, 104), shows that higher-order effects are negligible [$\mathcal{O}(10^{-12})$] for the accuracy needed at present.

4.4. Summary

Table 2 collects the various SM contributions to a_μ that are discussed above. Note that the largest error at present is that from the lowest-order HVP contribution. Addition of the experimental and theoretical errors in quadrature gives a total of

$$a_\mu^{\text{SM}} = (116\ 591\ 801 \pm 49) \times 10^{-11}, \qquad 28.$$

with an overall uncertainty that is slightly smaller than the one in the experimental determination in Equation 4. Comparison between these two numbers reveals a 3.6-σ discrepancy. If instead of the determination of a_μ^{HVP} in Equation 11 we use the one in Equation 12, the discrepancy is reduced to 3.2 σ—still very significant.

Table 2 SM contributions

Contribution	Result in 10^{-11} units
QED (leptons)	$116\,584\,718.09 \pm 0.15$
HVP(lo)$[e^+e^-]$	$6\,923 \pm 42$
HVP(ho)	-98.4 ± 0.7
HLbyL	105 ± 26
EW	153 ± 1
Total SM	$116\,591\,801 \pm 49$

Abbreviations: EW, electroweak; HLbyL, hadronic light-by-light scattering; ho, highest order; HVP, hadronic vacuum polarization; lo, lowest order; SM, Standard Model.

5. BEYOND THE STANDARD MODEL

The muon magnetic moment is sensitive not only to all interactions of the SM but also to potential physics beyond the SM (BSM). BSM physics could be the origin of the currently observed deviation (Equation 6), and a_μ provides a useful constraint on BSM physics.

5.1. Different Types of Contributions

Both the muon mass and a_μ correspond to terms in the Lagrangian or effective action that are chirality flipping; that is, they convert a left-handed muon into a right-handed muon. For this reason, New Physics contributions to the muon mass and to a_μ are linked by a general relation, discussed by Czarnecki & Marciano (105). If new particles with mass scale Λ contribute to the muon mass $\delta m_\mu(\text{N.P.})$, then there are corresponding Feynman diagrams contributing to a_μ, and the two contributions are related as follows:

$$a_\mu(\text{N.P.}) = \mathcal{O}(1) \times \left(\frac{m_\mu}{\Lambda}\right)^2 \times \left(\frac{\delta m_\mu(\text{N.P.})}{m_\mu}\right). \qquad 29.$$

This relation is model independent, but the value of the constant $C = \delta m_\mu(\text{N.P.})/m_\mu$ is highly model dependent. It is important that the $\mathcal{O}(1)$ factors not contain any coupling constants or $1/16\pi^2$ factors—those are contained in the constant C. A first consequence of this relation is that New Physics can explain the currently observed deviation only if Λ is at the TeV scale or smaller (assuming no fine-tuning in the muon mass; $|C| \leq 1$).

Second, the relation illustrates how very different contributions to a_μ are possible.

1. For models with new weakly interacting particles [e.g., Z', W', little Higgs, or universal extra-dimension models (106, 107)], one typically obtains perturbative contributions to the muon mass: $C = \mathcal{O}(\alpha/4\pi)$. Therefore, these models predict very small contributions to a_μ and might be challenged by a future, more precise a_μ measurement.
2. For supersymmetric (SUSY) models, one obtains an additional factor, $\tan\beta$, which is the ratio of the two Higgs vacuum expectation values (36). A numerical approximation for the SUSY contributions is given by

$$a_\mu^{\text{SUSY}} \approx 13 \times 10^{-10} \left(\frac{100\ \text{GeV}}{M_{\text{SUSY}}}\right)^2 \tan\beta\ \text{sign}(\mu), \qquad 30.$$

where M_{SUSY} denotes the common superpartner mass scale and μ is the Higgsino mass parameter. This value agrees with the generic result in Equation 29 for $C = \mathcal{O}(\tan\beta \times \alpha/4\pi)$ and is exactly valid if all SUSY masses are equal to M_{SUSY}. In other cases, M_{SUSY} must be replaced by a complicated combination of the relevant smuon, sneutrino, chargino, and

neutralino masses. The formula shows that the observed deviation could be explained, for instance, for relevant SUSY masses of roughly 200 GeV and $\tan\beta \sim 10$ or for SUSY masses of 500 GeV and $\tan\beta \sim 50$. However, the SUSY prediction for a_μ depends strongly on the detailed scenario, and if SUSY exists, then a_μ will help measure the SUSY parameters. Similarly to SUSY, Randall–Sundrum models (110–112) and large extra-dimension models (113) can provide enhanced contributions to a_μ.

3. Models with $C \simeq 1$ are of interest because the muon mass is given essentially by New Physics loop effects. Some examples of such radiative muon mass generation models are given in Reference 105. For examples within SUSY see, for example, References 108 and 109. In such models, a_μ can be large even for particle masses at the TeV scale.

5.2. a_μ as a Constraint on Physics Beyond the Standard Model

The importance of a_μ as a constraint on BSM physics arises primarily from two facts (114). First, because different types of BSM physics can contribute to a_μ by very different amounts, as discussed above, a_μ constitutes a meaningful benchmark and discriminator between BSM models. Second, the constraints from a_μ on BSM models are different and complementary to constraints from other observables from low- or high-energy measurements.

The complementarity between a_μ and other observables can be easily demonstrated. a_μ corresponds to a flavor- and *CP*-conserving interaction that is sensitive to chirality flips. Many other low-energy observables are chirality flipping but flavor violating (e.g., b or K decays, $\mu \to e$ conversion) or *CP* violating (EDMs). In particular, the LHC experiments are sensitive mainly to new strongly interacting particles, whereas a_μ is sensitive to weakly interacting new particles that interact with muons.

Below, we concentrate on the case of SUSY, arguably the most promising BSM explanation of the observed deviation (Equation 6). **Figure 12** illustrates the complementarity between LHC and a_μ for the case of SUSY.

Figure 12a shows that the SUSY contributions to a_μ are indeed very model dependent. The values for the so-called SPS benchmark points (116) range considerably and can be positive and negative because of the factor sign (μ) in Equation 30; note that this sign would be particularly difficult to determine at the LHC even if SUSY were to be discovered. The discriminating power of the current and improved measurements is evident in **Figure 12a**. One might think that if SUSY exists, the LHC experiments will detect it and measure its parameters. However, this is not necessarily the case. **Figure 12a** shows the "degenerate solutions" from Reference 117, which are different SUSY parameter points that cannot be distinguished at the LHC alone (also see Reference 118 for the LHC inverse problem). They have very different a_μ predictions; therefore, a_μ will resolve such LHC degeneracies.

Figure 12b illustrates that the SUSY parameter $\tan\beta$ can be measured more precisely by combining LHC data with a_μ. This figure is based on the assumptions that SUSY is realized in nature, found at the LHC, and constitutes the origin of the observed a_μ deviation (Equation 6). As a specific example, we use a slightly modified SPS1a benchmark point with $\tan\beta$ scaled down to $\tan\beta = 8.5$ such that a_μ^{SUSY} is equal to an assumed deviation of $\Delta a_\mu = 255 \times 10^{-11}$.[9] Mass measurements at the LHC alone are sufficient to determine $\tan\beta$ to a precision of ± 4.5 only (115). In such a situation one can study the SUSY prediction for a_μ as a function of $\tan\beta$ (all

---

[9]The actual SPS1a point is ruled out by the LHC; however, for our purposes only, the weakly interacting particles are relevant and are not excluded. The following conclusions are not very sensitive either to the actual $\tan\beta$ value or to the actual value of the deviation Δa_μ.
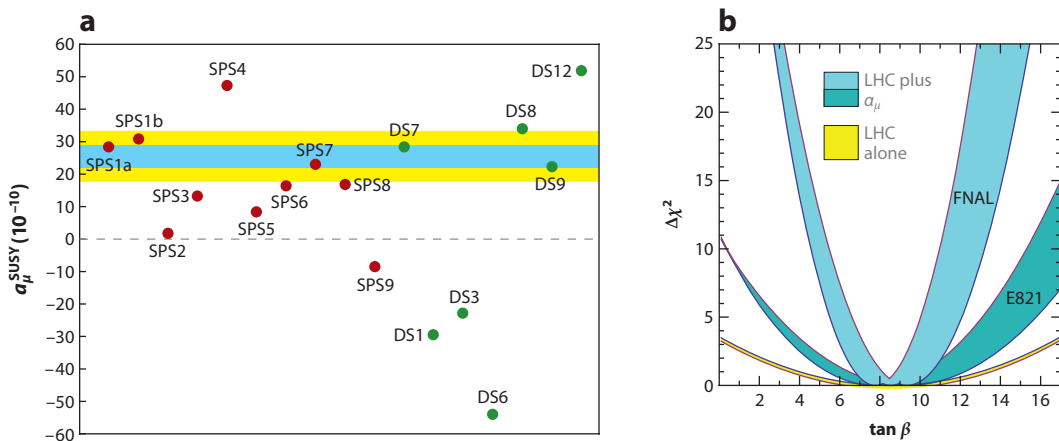
Figure 12

(*a*) Supersymmetric (SUSY) contributions to a_μ for the SPS benchmark points (*red*) and for the "degenerate solutions" from Reference 117. (*b*) Possible future $\tan\beta$ determination assuming that a slightly modified minimal supersymmetric Standard Model point SPS1a is realized. The bands show the $\Delta\chi^2$ parabolas from LHC data alone (*yellow*) (115), including the a_μ with the current precision (*dark blue*) and with the prospective precision (*light blue*). The width of the blue curves results from the expected LHC uncertainty of the parameters (mainly smuon and chargino masses) (115).

other parameters are known from the global fit to LHC data) and compare it with the measured value, in particular after an improved measurement. The figure compares the LHC $\Delta\chi^2$ parabola with the ones obtained by including a_μ, $\Delta\chi^2 = [(a_\mu^{\mathrm{SUSY}}(\tan\beta) - \Delta a_\mu)/\delta a_\mu]^2$, with the errors $\delta a_\mu = 80 \times 10^{-11}$ and 34×10^{-11}. Use of the current precision for a_μ would already improve the determination of $\tan\beta$, but the improvement will be even more impressive after a future, more precise a_μ measurement.

In recent years, a_μ has been one of the most important constraints on SUSY, next to the dark matter density, observables from b physics, and direct searches for Higgs and SUSY particles. LHC experiments have already excluded significant SUSY parameter regions. It is still possible to reconcile a_μ with LHC data even within the most restricted SUSY scenarios (119, 120). However, the negative LHC searches create a tension because a_μ prefers light, weakly interacting SUSY particles, whereas LHC data place stringent lower limits on the masses of strongly interacting SUSY particles. Apart from theoretical arguments related to naturalness and EW symmetry breaking, a_μ is the main driver for the expectation of a (at least partially) rather light SUSY spectrum, and it will be very useful to confront the future LHC results with the future a_μ measurements.

6. SUMMARY AND OUTLOOK

The measurement and theory of MDMs have been intertwined with the development of the modern physics of the twentieth century. The muon MDM, in particular, has played an important role in forcing theorists to grapple with ever-higher orders of QED, with hadronic contributions to lepton properties, and with EW contributions through two loops. The chiral nature of the MDM interaction probes New Physics in a way that is complementary to experiments at the LHC, and the E821 result and its successors will constrain the interpretation of whatever New Physics is discovered there.

The hint of BSM physics from E821 has motivated an enormous amount of work in the theoretical and experimental communities to understand the hadronic contributions to the SM value of

a_μ, which continues today. Additional e^+e^- data will be collected in Frascati, Novosibirsk, Beijing, and KEK and will further improve the hadronic contributions. The lattice is beginning to come into its own in contributing not only to the calculation of the lowest-order HVP but also, we hope, to the understanding of the contribution from HLbyL. The new muon $(g-2)$ experiment, E989 at Fermilab, is progressing with a goal of four-times-better precision. The J-PARC Collaboration is also moving forward on critical R&D items that are necessary to demonstrate that this alternate technique can work. The new $(g-2)$ experiments, along with the charged-lepton flavor-violating searches under way at PSI, Fermilab, and J-PARC, are a key part of the intensity frontier program worldwide, which will provide an important complement to the energy frontier program.

DISCLOSURE STATEMENT

The authors are not aware of any affiliations, memberships, funding, or financial holdings that might be perceived as affecting the objectivity of this review.

ACKNOWLEDGMENTS

LITERATURE CITED

1. Stern O. *Z. Phys.* 7:249 (1921)
2. Gerlach W, Stern O. *Z. Phys.* 8:110 (1922); Gerlach W, Stern O. *Z. Phys.* 9:349 (1922); Gerlach W, Stern O. *Z. Phys.* 9:353 (1924)
3. Gerlach W, Stern O. *Ann. Phys.* 74:673 (1924)
4. Uhlenbeck GE, Goudsmit S. *Naturwissenschaften* 47:953 (1925)
5. Uhlenbeck GE, Goudsmit S. *Nature* 117:264 (1926)
6. Schrödinger E. *Ann. Phys.* 79:361 (1926)
7. Thomas LH. *Nature* 117:514 (1926); Thomas LH. *Phil. Mag.* 3:1 (1927)
8. Dirac PAM. *Proc. R. Soc. Lond. A* 117:610 (1928); Dirac PAM. *Proc. R. Soc. Lond. A* 118:351 (1928); Dirac PAM. *The Principles of Quantum Mechanics.* London: Oxford Univ. Press. 4th ed. (1958)
9. Pais A. *Paul Dirac: The Man and His Work*, ed. P Goddard. New York: Cambridge Univ. Press (1998)
10. Phipps TE, Taylor JB. *Phys. Rev.* 29:309 (1927)
11. Purcell EM, Ramsey NF. *Phys. Rev.* 78:807 (1950)
12. Landau L. *Nucl. Phys.* 3:127 (1957)
13. Ramsey NF. *Phys. Rev.* 109:225 (1958)
14. Pospelov P, Ritz A. *Ann. Phys.* 318:119 (2005); Pospelov P, Ritz A. In *Lepton Dipole Moments*, ed. BL Roberts, WJ Marciano, p. 439. Singapore: World Sci. (2010)
15. Nafe JE, Nelson EB, Rabi II. *Phys. Rev.* 71:914 (1947)
16. Nagel DE, Julian RS, Zacharias JR. *Phys. Rev.* 72:971 (1947)
17. Kusch P, Foley HM. *Phys. Rev.* 72:1256 (1947)
18. Schwinger J. *Phys. Rev.* 73:416L (1948); Schwinger J. *Phys. Rev.* 76:790 (1949)
19. Kusch P, Foley HM. *Phys. Rev.* 73:250 (1948)
20. Bethe HA, Salpeter EE. *Quantum Mechanics of One- and Two-Electron Atoms.* Berlin: Springer (1957)
21. Garwin RL, Lederman LM, Weinrich M. *Phys. Rev.* 105:1415 (1957)
22. Garwin RL, Hutchinson DP, Penman S, Shapiro G. *Phys. Rev.* 118:271 (1960)
23. Charpak G, et al. *Phys. Rev. Lett.* 6:28 (1961); Charpak G, et al. *Nuovo Cim.* 22:1043 (1961); Charpak G, et al. *Phys. Lett.* 1:16 (1962); Charpak G, et al. *Nuovo Cim.* 37:1241 (1965)
24. Bailey J, et al. *Phys. Lett. B* 28:287 (1968); Bailey J, et al. *Nuovo Cim. A* 9:369 (1972)

25. Bailey J, et al. *Nucl. Phys. B* 150:1 (1979)
26. Bargmann V, Michel L, Telegdi VL. *Phys. Rev. Lett.* 2:435 (1959)
27. Mohr PJ, Taylor BN, Newell DB. *Rev. Mod. Phys.* 80:633 (2008)
28. Bennett GW, et al. (*g* − 2 Collab.) *Phys. Rev. Lett.* 92:161802 (2004)
29. Bennett GW, et al. (*g* − 2 Collab.) *Phys. Rev. D* 73:072003 (2006)
30. Davier M, et al. *Eur. Phys. J.* C 71:1515 (2011)
31. Miller JP, de Rafael E, Roberts BL. *Rep. Prog. Phys.* 70:795 (2007)
32. Roberts BL, Marciano WJ, eds. *Advanced Series on Directions in High Energy Physics*, vol. 20: *Lepton Dipole Moments*. Singapore: World Sci. (2010)
33. Miller JP, Roberts BL, Jungman K. See Ref. 32, p. 333 (2010)
34. Prades J, de Rafael E, Vainshtein A. See Ref. 32, p. 303 (2010)
35. Stöckinger D. See Ref. 32, p. 393 (2010)
36. Stöckinger D. *J. Phys. G* 34:R45 (2007)
37. Yamamoto A, et al. *Nucl. Instrum. Methods A* 491:23 (2002)
38. Efstathiadis E, et al. *Nucl. Instrum. Methods A* 496:8 (2002)
39. Carey RM, et al. (*g*−2 Collab.) *Phys. Rev. Lett.* 82:1632 (1999)
40. Semertzidis YK, et al. *Nucl. Instrum. Methods A* 503:458 (2003)
41. Sedykh SA, et al. *Nucl. Instrum. Methods A* 455:346 (2000)
42. Danby GT, et al. *Nucl. Instrum. Methods A* 457:151 (2001)
43. Prigl R, et al. *Nucl. Instrum. Methods A* 374:118 (1996)
44. Fei X, Hughes V, Prigl R. *Nucl. Instrum. Methods A* 394:349 (1997)
45. Abragam A. In *Principles of Nuclear Magnetism*, p. 173. New York: Oxford Univ. Press (1961)
46. Mohr PJ, Taylor BH. *Rev. Mod. Phys.* 77:1 (2005)
47. Phillips WD, et al. *Metrologia* 13:179 (1979)
48. Winkler PF, Kleppner D, Myint T, Walther FG. *Phys. Rev. A* 5:83 (1972)
49. Lamb WE Jr. *Phys. Rev.* 60:817 (1941)
50. Grotch H, Hegstrom RA. *Phys. Rev. A* 4:59 (1971)
51. Petley BW, et al. *Metrologia* 20:81 (1984)
52. Bennett GW, et al. (*g*−2 Collab.) *Phys. Rev. D* 80:052008 (2009)
53. Carey R, et al. *FERMILAB-PROPOSAL-0989*. **http://lss.fnal.gov/archive/test-proposal/0000/fermilab-proposal-0989.shtml** (1989)
54. Mibe T. *Nucl. Phys. B* (*Proc. Suppl.*) 218:242 (2011)
55. Jegerlehner F, Nyffeler A. *Phys. Rep.* 477:1 (2009)
56. Petermann A. *Helv. Phys. Acta.* 30:407 (1957); Petermann A. *Nucl. Phys.* 5:677 (1958)
57. Sommerfield CM. *Phys. Rev.* 107:328 (1957); *Ann. Phys.* 5:26 (1958)
58. Laporta S, Remiddi E. *Phys. Lett. B.* 379:283 (1996)
59. Aoyama T, Hayakawa M, Kinoshita T, Nio M. *Phys. Rev. Lett.* 99:110406 (2007)
60. Aoyama T, Hayakawa M, Kinoshita T, Nio M. arXiv:1201.2461 [hep-ph] (2012)
61. Hanneke D, Fogwell S, Gabrielse G. *Phys. Rev. Lett.* 100:120801 (2008)
62. Laporta S. *Nuovo Cim. A* 106:675 (1993)
63. Laporta S, Remiddi E. *Phys. Lett. B* 301:440 (1993)
64. Passera M. *J. Phys. G* 31:75 (2005)
65. Aguilar J-Ph, de Rafael E, Greynat D. *Phys. Rev. D* 77:093010 (2008)
66. Kinoshita T, Nio M. *Phys. Rev. D* 70:113001 (2004)
67. Kinoshita T, Nio M. *Phys. Rev. D* 73:053007 (2006)
68. Bouchiat C, Michel L. *J. Phys. Radium* 22:121 (1961)
69. Gourdin M, de Rafael E. *Nucl. Phys. B* 10:667 (1969)
70. Bell JS, de Rafael E. *Nucl. Phys. B* 11:611 (1969)
71. Hagiwara K, et al. *J. Phys. G* 38:085003 (2011)
72. Jegerlehner F, Szafron R. *Eur. Phys. J. C* 71:1632 (2011)
73. Benayoun M, David P, DelBuono L, Jegerlehner F. arXiv:1107.4683 [hep-ph] (2011)
74. Calmet J, Narison S, Perrottet M, de Rafael E. *Phys. Lett. B* 61:283 (1975)
75. Brodsky S, de Rafael E. *Phys. Rev.* 168:1620 (1968)

76. Lautrup BE, de Rafael E. *Phys. Rev.* 174:1835 (1968)
77. Barbieri R, Remiddi E. *Nucl. Phys. B* 90: 997 (1975)
78. Lautrup BE, Peterman A, de Rafael E. *Phys. Rep. C* 3:193 (1972)
79. de Rafael E. *Phys. Lett. B* 322:239 (1994)
80. Feng X, Jansen K, Petschlies M, Renner DB. *Phys. Rev. Lett.* 107:081802 (2011)
81. Aldins J, Brodsky S, Dufner A, Kinoshita T. *Phys. Rev. Lett.* 23:441 (1969); Aldins J, Brodsky S, Dufner A, Kinoshita T. *Phys. Rev. D* 1:2378 (1970)
82. Knecht M, Nyffeler A, Perrottet M, de Rafael E. *Phys. Rev. Lett.* 88:071802 (2002)
83. Knecht M, Nyffeler A. *Phys. Rev. D* 65:073034 (2002)
84. Ramsey-Musolf M, Wise MB. *Phys. Rev. Lett.* 89:041601 (2002)
85. Melnikov K, Vainshtein A. *Phys. Rev. D* 70:113006 (2004)
86. Knecht M, Peris S, Perrottet M, de Rafael E. *J. High Energy Phys.* 0211:003 (2002)
87. Vainshtein A. *Phys. Lett. B* 569:187 (2003)
88. Knecht M, Peris S, Perrottet M, de Rafael E. *J. High Energy Phys.* 0403:035 (2004)
89. Hayakawa M, Kinoshita T. Erratum. *Phys. Rev. D* 66:073034 (2002)
90. Bijnens J, Pallante E, Prades J. *Nucl. Phys. B* 626:410 (2002)
91. Bartos E, et al. *Nucl. Phys. B* 632:330 (2002)
92. Nyffeler A. *Phys. Rev. D* 79:073012 (2009)
93. Cappiello L, Catà O, D'Ambrosio G. *Phys. Rev. D* 83:093006 (2011)
94. Dorokhov AE, Radzhabov AE, Zhevlakov AS. *Eur. Phys. J. C* 71:1702 (2011)
95. Goecke T, Fisher ChS, Williams R. *Phys. Rev. D* 83:094006 (2011)
96. Engel KT, Patel HH, Ramsey-Musolf MJ. arXiv:1201.0809v2 [hep-ph] (2012)
97. Bardeen WA, Gastmans R, Lautrup BE. *Nucl. Phys. B* 46:315 (1972)
98. Czarnecki A, Krause A, Marciano W. *Phys. Rev. D* 52:2619 (1995); Czarnecki A, Krause A, Marciano W. *Phys. Rev. Lett.* 76:3267 (1996)
99. Heinemeyer S, Stöckinger D, Weiglein G. *Nucl. Phys. B* 699:103 (2004)
100. Gribouk T, Czarnecki A. *Phys. Rev. D* 72:053016 (2005)
101. ATLAS Collab., CMS Collab. *ATLAS-CONF-2011-157, CMS PAS HIG-11-023.* **http://cdsweb.cern.ch/record/1399599/files/ATLAS-CONF-2011-157.pdf** (2011)
102. Peris S, Perrottet M, de Rafael E. *J. High Energy Phys.* 05:011 (1998)
103. Czarnecki A, Marciano WJ, Vainshtein A. *Phys. Rev. D* 67:073006 (2003); Czarnecki A, Marciano WJ, Vainshtein A. Erratum. *Phys. Rev. D* 73:119901 (2006)
104. Degrasi G, Giudice GF. *Phys. Rev. D* 58:053007 (1998)
105. Czarnecki A, Marciano WJ. *Phys. Rev. D* 64:013014 (2001)
106. Blanke M, et al. *J. High Energy Phys.* 0705:013 (2007); Blanke M, et al. arXiv:hep-ph/0702136 (2010)
107. Appelquist T, Dobrescu BA. *Phys. Lett. B* 85:516 (2001); Appelquist T, Dobrescu BA. arXiv:hep-ph/0106140 (2001)
108. Borzumati F, Farrar GR, Polonsky N, Thomas SD. *Nucl. Phys. B* 53:555 (1999)
109. Crivellin A, Girrbach J, Nierste U. *Phys. Rev. D* 83:055009 (2011); Crivellin A, Girrbach J, Nierste U. arXiv:1010.4485 [hep-ph] (2011)
110. Davoudiasl H, Hewett JL, Rizzo TG. *Phys. Lett. B* 493:135 (2000)
111. Park SC, Song HS. *Phys. Lett. B* 506:99 (2001)
112. Kim CS, Kim JD, Song JH. *Phys. Lett. B* 511:251 (2001)
113. Graesser ML. *Phys. Rev. D* 61:074019 (2000)
114. Hertzog DW, et al. arXiv:0705.4617 [hep-ph] (2007)
115. Alexander M, et al. arXiv:0802.3672 [hep-ph] (2008)
116. Allanach BC, et al. *Eur. Phys. J. C* 25:113 (2002)
117. Adam C, et al. *Eur. Phys. J. C* 71:1520 (2011)
118. Arkani-Hamed N, Kane GL, Thaler J, Wang LT. *J. High Energy Phys.* 0608:070 (2006)
119. Bechtle P, et al. *Phys. Rev. D* 84:011701 (2011)
120. Buchmueller O, et al. arXiv:1110.3568 [hep-ph] (2011)

A̲R̲

Contents

Indexes

Errata

An online log of corrections to *Annual Review of Nuclear and Particle Science* articles may
be found at http://nucl.annualreviews.org/errata.shtml